Applied Surface Science 478 (2019) 818–830

Contents lists available at ScienceDirect

Applied Surface Science

journal homepage: www.elsevier.com/locate/apsusc

Full length article

Transport properties of liquid metals and semiconductors from molecular dynamics simulation with the Kubo-Greenwood formula

K.P. Migdal[a,b,*], V.V. Zhakhovsky[a,b], A.V. Yanilkin[a], Yu.V. Petrov[b,c], N.A. Inogamov[a,b]

[a] Dukhov Research Institute of Automatics (VNIIA), 22 Sushchevskaya Street, Moscow 127055, Russian Federation
[b] Landau Institute for Theoretical Physics, Russian Academy of Science, 1a Akademika Semyonova Street, Chernogolovka 142432, Moscow region, Russian Federation
[c] Moscow Institute of Physics and Technology, 8 Institutskaya Street, Dolgoprudnyi, Moscow region 141700, Russian Federation

ARTICLE INFO

Keywords:
Laser melting
Femtosecond laser pulses
Nanosecond laser pulses
Electron transport

ABSTRACT

Short but intense laser pulses may produce the high surface temperatures of metal or semiconductor targets exceeding the corresponding melting points. Hydrodynamic modeling of nano-scale fragmentation of a thin surface layer is feasible if the reflectivity and heat conductivity coefficients, usually obtained from experiments, are available. However, for such materials as silicon and titanium the experimental electric resistivity and heat conductivity are available only in narrow temperature ranges above the melting points. On the other hand, the heated surface layer keeps its initial density during a short two-temperature stage because the timescales of both femtosecond laser heating and electron-ion energy exchange are too short for material expansion. The short-lived high-temperature states of materials in this layer are also challenging for experimental study with techniques such as electrical explosion of wires or films.

We perform accurate simulations of several materials in such states, including aluminum, copper, gold, silicon, and titanium, at the corresponding equilibrium volumes at room temperature and along their liquid-vapor coexistence curves using both classical and quantum molecular dynamics. The corresponding electron transport properties calculated by the Kubo-Greenwood theory are presented.

1. Introduction

Nano- and femtosecond laser pulses are used in many technologies to act on surfaces of metals or semiconductors, where surface treatment or transfer of material is required [1,2]. To cite a few examples for illustrative purposes: formation of nano-antenna arrays on the metal surface as emitters at surface plasmon resonance [3,4], producing of similar nanostructures on silicon [5-7], modification of the optical and mechanical surface properties at the meso- and macroscale by femtosecond pulses [8], as well as a spark discharge in fuses by nanosecond pulses [9,10] and production of nano-particles via phase explosion [11]. Also, irradiation with femtosecond pulses is one of the primary methods for experimental investigations of “hot-dense” matter, which is of fundamental importance for the physics of planets and inertial thermonuclear fusion [12-14].

After moderate laser irradiation within a relatively long duration in the range of 10^{-7}–10^{-11} s, a significant change in the temperature of substance and/or its density occurs in the heating surface layer. For the nanosecond laser pulses, the heating of the surface layer takes a longer time than the characteristic duration of electron-ion relaxation and acoustic unloading of stresses generated by heating. Due to this, the heating in the surface layer takes place simultaneously in both the electron and ion subsystems, which is accompanied by the isobaric expansion.

But for femtosecond irradiation, the energy exchange between hot electrons and cold ions takes place during approximately 1–10 ps while the material density changes only slightly. For absorbed laser fluences typical for the frontal ablation, the electron temperature decreases from several eV to thousands of Kelvin, becoming one order with the ion temperature. Because this, two-temperature evolution of material state lasts several picoseconds, the experimental diagnostics of the heated layer has a number of limitations, among which the spatial and time resolutions, and the possibility of studying the states in the bulk. The time resolution of the order of 100 fs can be achieved by using the “pump-probe” method [15]. Recently, the experimental analysis of the material states within a few micrometer layer is being performed in Refs.[16,17] with using X-ray diffraction techniques.

Two-temperature modeling [18,19] is often used as a more accessible and convenient method to obtain the necessary description of laser-initiated processes. It requires many parameters of the material in

---

[*] Corresponding author.
E-mail address: migdal@vniia.ru (K.P. Migdal).

https://doi.org/10.1016/j.apsusc.2019.01.293
Received 17 September 2018; Received in revised form 30 December 2018; Accepted 31 January 2019

the two-temperature states, which may differ significantly from the equilibrium values. It is also necessary to have a wide-range equation of state and to know the contribution of the hot electron subsystem to both the thermodynamic and transport properties [19-21].

In the framework of thermodynamic perturbation theory [22,23], it is possible to consider electron thermodynamic potentials as functions of electron temperature only. The most commonly used approaches [24,25] for the problem of electron-phonon heat transfer demonstrate that the heat transfer rate divided on the difference of two temperatures is independent of the ion temperature. Thus, a new model should be developed for calculation of the two-temperature heat conductivity considered as a function of three parameters: density and two temperatures.

There is a number of approaches to this problem, ranging from simple analytic expressions of the form $T_e/(aT_e^2 + bT_i)$ [26], which corresponds to the low-temperature electron properties according to the Drude model, as well as the empirical formula " 5/4" [27], which uses a more complex but still fixed functional form for all metals characterized by two arbitrary parameters C and β:

$$\varkappa_{5/4} = C\frac{((T_e/T_F)^2 + 0.16)^{5/4}\sqrt{(T_e/T_F)^2 + 0.44}\,(T_e/T_F)}{\sqrt{(T_e/T_F)^2 + 0.092}\,((T_e/T_F)^2 + \beta T_i)}, \tag{1}$$

where T_F is the Fermi temperature of free electron gas in a metal. Investigations of electron transport properties in two-temperature states [28-32] show the good agreement with the experimental data measured at the equilibrium temperature. But contrary to the prediction of the well-known " 5/4" model, Refs. [29,31] demonstrate that the electron heat conductivity increases linearly with the electron temperature.

These methods show poor agreement with the calculations via the Kubo-Greenwood theory in many examples, even if we consider the qualitative behavior of heat conductivity with increasing electron and ion temperatures [30,31].

To address this issue, we used previously the solution of the Boltzmann kinetic equation in the relaxation-time approximation [33], which is found to be in good agreement with the first-principles Kubo-Greenwood calculations [30,21]. However, this approach has two assumptions that require verification. First, the experimental electric resistivity, retrieved by the Drude model, were widely used for determination of the electron-ion collision frequency. Here, the main question is how the deviation of density from initial equilibrium one disturbs the results of data retrieval. Secondly, the solution of the Boltzmann kinetic equation for electron-electron collisions is beyond the formal applicability conditions, because the average changes of the electron momenta after such a collision may be comparable with their initial values. The latter violates the basic assumptions used in the relaxation-time approximation [34]. To verify the applicability of these assumptions, it makes sense to calculate the electron heat conductivity for a list of materials of interest using a method combining the possibilities of quantum molecular dynamics (QMD) to simulate the two-temperature states with the Kubo-Greenwood formula taking into account electron-electron collisions [35].

In this paper, we applied this method to investigate the equilibrium and two-temperature states of hot materials at their normal densities. Presently such states are studied experimentally in electric explosion of wires and foils 36,37], which allows us to verify the conclusions of these works. In the next section, we present the main details of the used first-principles calculation method, where in the second subsection the special attention is paid to convergence of our results with the computational cell size for copper. Previously obtained results of the convergence test demonstrated by Knyazev [38] show that even for such a simple metal as aluminum the achievement of size convergence is limited by presently available computational resources. Next in Section 3, we show the test for copper to compare with our earlier results [33] with the data of the first-principles approach for the total frequency of electron collisions at variable electron and ion temperatures. Then, the main group of results for isochores at normal densities of copper and gold are presented. The calculated properties of stretched metals and semiconductors (Al, Cu, Si, Ti) are given afterward, where a dependence on the used exchange-correlation functional is specially investigated for silicon.

Table 1
The details of the QMD and Kubo-Greenwood calculations.

Metal	Al	Au	Cu	Si	Ti
Ionic timestep, fs	1	2	1.5	1	1
Number of valence, e^-	3	11	11	4	10
Empty states per atom	3.2	10	10	6	8
Smearing of δ-function, eV	0.1	0.1	0.1	0.2	0.15
Number of atoms in the computational cell	500	128	128	64	128

2. Computational methods

2.1. Scheme for calculation of transport properties

Computational package VASP [39,40] was used. Initially, the ideal lattice of the substance was considered, which was then heated to the target temperature using the Nose-Hoover thermostat. The duration of a heating stage was set on 1000 steps if the target temperature exceeded 4000 K. In another case, the first heating was carried out up to 4000 K, and then cooling also with a thermostat for 1000 steps. The step value varied with the material under consideration. It is shown in Table 1. After the melting was completed, a set of configurations was selected at the stage where the system was in the NVE ensemble. For each thermodynamic state for which the heat conductivity has been evaluated, there were at least five atomic configurations that were spaced from each other at least by 50 steps. The duration of this stage was set on 300 steps.

The electron wave functions in the framework of the density functional theory (DFT) used in QMD calculations were reproduced using the projected augmented waves (PAW) approach [41]. The exchange-correlation interaction was described in the generalized gradient approximation [42]. To this aim, the PAW-potentials library included in the VASP package was used. The number of electrons per atom considered as valence is given in Table 1. At the stages of heating and equilibration in NVE ensemble, the electron structure was reproduced by only 1 Γ-point in the computational cell. This simplification allowed us to use the version of VASP optimized for Γ-point calculations. The number of empty electron states was taken to ensure the convergence of the transport properties. Its value for material is also shown in Table 1.

In the case of titanium, a version of the PAW potential was used, where in addition to valence $3d^2 4s^2$ electrons, the $3p^6$ band separated from valence bands by a rather narrow gap was considered by the same basis. This version was chosen to provide accuracy of the calculation of the forces which is enough to determine the finally calculated atomic configurations.

The final calculation of transport properties using the Kubo-Greenwood formula was also carried out using the VASP package [43]. At first, one-electron wave functions and self-energies were calculated, as well as the occupation numbers. For this purpose, a more detailed grid of Monkhorst-Pack points was used. The k-grid dimension varied depending on the number of atoms and is given for each material in Table 1. Other parameters (cutoff energy, the number of empty electron states) did not change in comparison with the QMD calculation. A direct calculation using the Kubo-Greenwood formula was carried out using a module for post-processing the results of VASP, developed by D. V. Knyazev [44,45]. This module allows us to calculate all components of Onsager matrix including non-diagonal ones. The latter can be useful at electron temperatures of the order of several 10, 000 K when the decrease in thermal conductivity due to thermoelectric effects takes place [31].

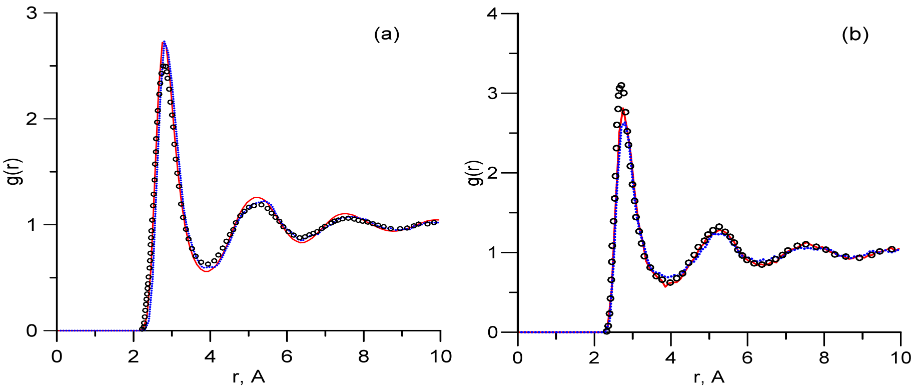

Fig. 1. Pair-correlation functions of Al and Au in the states close to the melting points. *a*: Aluminum at density of 2.35 g/cm^3 and temperature of 1000 K. Blue dashed line is used for the data of QMD calculation, red line corresponds to classical MD simulation, open circles represent the experimental result [46] at temperature of 973 K. *b*: Gold at density of 17 g/cm^3 and temperature of 2000 K. Used designations are the same as in Fig. 1 (a). Experimental data [47] had been obtained at temperature of 1423 K.

The smearing of the Gaussian function is responsible for the accuracy of the Fermi “golden rule”, which has the form of the Dirac function $\delta(\varepsilon_i - \varepsilon_j + \hbar\omega)$ in analytical calculations, where ε_i and ε_j are the one-electron energies between which the energy is changed by $\hbar\omega$. The smearing values providing a stable result are given in Table 1.

2.2. Determination of a proper atomic configuration

The diagnostics of the obtained atomic configurations was carried out with the help of the calculation of a pair-correlation function (PCF). For some thermodynamic states, there are data from experiments or previous calculations, which made it possible to compare the available data. In Figs. 1 and 2, the PCF‘s of the considered metals and liquid silicon is shown but copper which data are presented in the next section.

We can observe the good agreement of the PCF‘s presented in Fig. 1. Also, the PCF for titanium (see Fig. 2 (b)) found in the QMD calculation is in good agreement with the result of the experiment [48]. In the case of silicon represented in Fig. 2 (a), the situation is worse, since the calculation data have the good agreement with one of the two presented experimental results and only for the first coordination sphere [49]. Further correlations of the density are not in agreement with any one of the two experiments [49,50]. Obtained here results correspond to their rapid attenuation after the first peak, as takes place at the temperatures near critical points of metals [51,52]. At the end of this section, we will provide a test for silicon where some hybrid functionals are used for determination of electronic wave functions.

The cell size was determined as a compromise between the requirement to check the convergence of the result and the computational capabilities. In the case of aluminum, where there are only 1500 electrons in the cell. Thus, the calculation can be carried out with 500 atoms. Considering the data [38], we can claim that this value can be considered as reliable, because the values obtained at 256, 500, and 1372 atoms in the work [38] are quite close. Here we take into account the fact that the smearing defined in this work differs from the data of Ref. [38], where a jump in the conductivity value occurred after reaching 500 atoms together with a decrease in the smearing value. In the cases of gold, copper, and titanium, we have to deal with a large number of electrons. Although in the next section we show that there is a principal opportunity to carry out a calculation with the value of the number of atoms greater than 1000, we immediately note that this test provided for one thermodynamic state ($T_e = T_i = 2000$ K, 8 g/cm^3) was more time-consuming than all other calculations of heat conductivity of four metals. At the moment, we consider the limit size of the computational cell of liquid noble metals to be in order of 100 atoms in the case of serial calculations.

As it should be noted from Table 1, in the case of gold and copper the initial lattice corresponded to the base-centered cubic (bcc), rather than to the stable face-centered (fcc) symmetry. In the next subsection, where many types of copper configurations at the same ion and electron temperature as well as density have been studied, it will be demonstrated that the results for the transport coefficients are insensitive to a type of cubic lattice we specify: simple, bcc, or fcc. In other cases, those lattices that are stable under normal conditions were specified: fcc for aluminum, diamond-like for silicon and hexagonal close-packed (hcp) for titanium.

Reducing the computational resources consumed at quantum mechanical calculations of transport properties may also be achieved by using classical (MD) simulations rather than QMD ones. Omitting the question of the possibility of development of a two-temperature interatomic interaction potential, which is the subject of a particular scientific discussion [53], we will focus on the reproduction of an equilibrium state, including both the isochore of an equilibrium density (at T ≈ 300 K) and the binodal. To ensure this method is acceptable, we have carried out a number of calculations of the atomic configurations for aluminum and gold, obtained using both MD and QMD. We used previously developed potentials [54] based on the embedded-atom method.

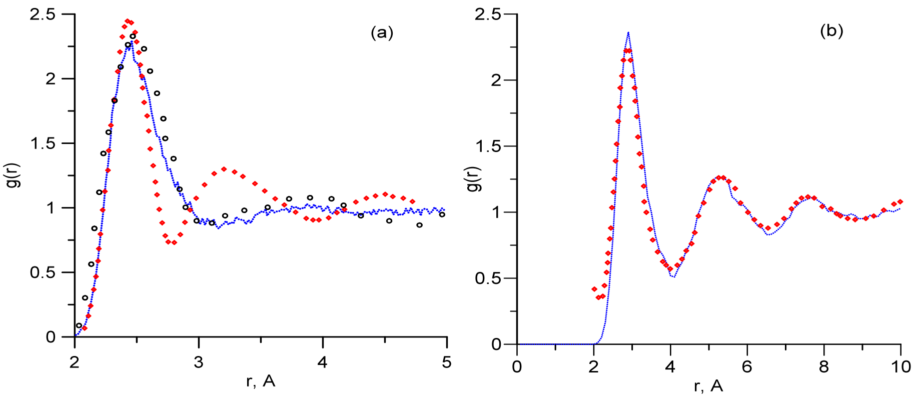

Fig. 2. Pair-correlation functions of Si and Ti in the states close to the melting points. *a*: Silicon at density of 2.59 g/cm^3 ^{3} and temperature of 1700 K. The result of QMD calculations is shown by blue dashed line, experimental data [49] are represented by open circles (T = 1758 K); red diamonds are used for the other experiment [50] (T = 1693 K). *b*: Titanium at density of 4.1 g/cm^3 and temperature of 2000 K. Blue dashed line corresponds to results of QMD calculations, experimental data [48] (T = 1965 K) red diamonds.

Atomic configurations in the thermodynamic states of interest were obtained by classical MD simulations in the LAMMPS [55] computational package. Also, as in the case of QMD calculations, the system was firstly heated from ideal lattice and melted, and then it was kept in the NVE ensemble to acquire atomic configurations. In the case of MD simulations, the time step was fixed at one fs. In contrast to the QMD calculations, longer runs were performed for the case of heating and melting with the NVT thermostat (500,000 steps instead of 1000) and also for the isolated system (300,000 and 300, respectively). This choice makes possible to select atomic configurations with the time delay of 50–70 ps between the neighbors, which is more than one for the QMD case on three orders of magnitude.

The data obtained from the MD calculations also enclose sets of 5 atomic configurations for each thermodynamic state. A comparison of the results for the pair-correlation function is shown in Fig. 1 (a) and (b).

2.3. Convergence with a cell size for a noble metal

According to the papers [31,38] dealt with the determination of aluminum transport properties at high temperatures, including two-temperature situation, the size of a computational cell should contain at least 256 atoms. In the case of noble metals, where one atom has significantly more valence electrons than three, the convergence check remains an urgent task. In previous works [56], authors attempted to observed convergence in copper at cell sizes from 27 to 108 atoms. In the work [56], this check was conducted for liquid copper at density of 8 g/cm^3 and temperature of 2000 K, which corresponds to a low compression with respect to the equilibrium state at a given temperature (7.5 g/cm^3). Calculation of the single-electron wave functions and energies, as well as the filling numbers, was carried out using both the PAW approach and the all-electron method FP-LAPW implemented in the computational code Elk [57]. The latter basis, increasing the computational complexity, allowed nevertheless to obtain a result that better corresponded to the experimental data on the electric resistivity of copper [58]. In this paper, we continue the discussed check using only the PAW method due to the restrictions on the memory used and the calculation time was reached for the all-electron approach in the previous work.

Providing this check, we would like not only to increase the size of the cell but also to consider three questions about probable simplifications of such a procedure. Firstly, in addition to the fcc cells used for copper, melting from lattices with other symmetries will also be considered. As mentioned in Section 2, if we consider temperatures below 4000 K, then we accelerate melting in NVT thermostat by heating up to 4000 K. Fast melting and subsequent cooling to a target temperature, occupying 2000 ion steps could make selected atomic configurations insensible to the original lattice. To verify this assumption, we compared the results obtained for the thermodynamic and transport properties of copper, considering the cells that initially had both fcc, bcc, and also simple cubic (SC) symmetries.

The second question is the effect of the shape of a computational cell if we are using parallelepiped with an arbitrary aspect ratio instead of a cubic cell. At calculations of the electron transport along each direction, we can see whether this effect is significant in comparison with the unavoidable calculation errors due to the convergence problem. We are interested in two possible deformations of the original cubic cell. The first one is a significant elongation of the cell along a one of directions to get a linear scale that we could not achieve using cubic cells. Our interest in this is related with a simple estimation between the sizes of a computational cell and a mean free path of electrons moving in the lattice. At low temperatures, the latter can reach the order of 10–100 nm in noble metals, which obviously cannot be reproduced in the QMD approach. Due to an increase in scattering rate of electrons with ion or electron temperatures, this parameter decreases to a few nanometers and becomes closer to the achievable linear scale of the computational cell.

On the contrary, the second deformation is the flattening of the cell into a thin slab. The object of this transformation, firstly, is in the lowering of a k-points number in an irreducible Brillouin zone, if we considering a density of the k-grid as a key parameter of QMD calculations with the same number of atoms in the cell. Secondly, in this case, we consider not only three-dimensional and quasi-one-dimensional but also quasi-two-dimensional structures.

A positive answer to the second question would mean that we can continue the convergence check focusing on the maximum linear scale for the computational cell rather than the simple number of atoms.

For more accurately reveal of the effect of the cell, we have chosen their sides in a way that provide a comparison the result for a cubic (or almost cubic) cell with the same number of atoms. We used elongated cells with a square cross-section having 112 (2 × 2 × 7), 176 (2 × 2 × 11) atoms, and also flattened cells with 128 (2 × 4 × 4), and 216 (3 × 8 × 9) atoms. Corresponding cubic cells had 108, 180 (5 × 6 × 6), and 216 atoms. Here, we implied that the previous assumption about the independence of the transport properties on the initial atomic arrangement had already obtained a positive response.

In Table 2, the parameters used for all the cells subjected to the convergence check are given.

According to the data of Table 2 provided for the cell sizes and corresponding k-grids, the density of the k-grid was maintained close to one value in all three directions. The density of the k-grid is lies between 0.1 and 0.15 Å^{-1}. This range of the k-grid density was established as a result of a convergence test carried out over a full range of cell sizes and for the case of non-cubic cells.

The smearing of the Gaussian function used in the Kubo-Greenwood formula was changed in comparison with Section 2 only in the case of the two largest cells. In the case of cells with 500 and 1372 atoms, it was 0.05 eV.

The number of empty electron states per atom was set to 8 for all the cases presented in Table 1.

According to Fig. 3, we can observe a convergence with the increasing number of atoms for both the types of computational cells. As shown in the left part of Fig. 3 significant differences from a rather smooth result corresponding to the cell with 1372 atoms are observed only in the smallest cells with 108 and 128 atoms. There are no any visible differences between the curves corresponding to 128 and 216 atoms in the cell, although the initial positions of the atoms in these cells did not correspond to fcc symmetry. If we consider Fig. 3 (b), we can see that for a sufficiently close number of atoms, the result obtained for 243 atoms are in better agreement with the experiment in the range of the second and third coordination spheres. This fact may be explained as a manifestation of a more significant number of neighbors inside the cell per atom in a quasi-two-dimensional case than in a quasi-one-dimensional one.

The comparison between the results for cubic and deformed cells, where the number of atoms was almost the same, is also of our interest.

Table 2
The considered computational cells.

Number of atoms in the cell	Lattice	Aspect ratio for the cell	k-grid	Smearing of δ-function, eV
108	fcc	3 × 3 × 3	4 × 4 × 4	0.1
112	fcc	2 × 2 × 7	6 × 2 × 2	0.1
128	bcc	4 × 4 × 4	4 × 4 × 4	0.1
128	fcc	2 × 4 × 4	6 × 4 × 4	0.1
176	fcc	2 × 2 × 11	6 × 6 × 3	0.1
180	sc	5 × 6 × 6	4 × 4 × 4	0.1
216	sc	6 × 6 × 6	4 × 4 × 4	0.1
216	sc	3 × 8 × 9	6 × 3 × 3	0.1
243	sc	3 × 9 × 9	6 × 3 × 3	0.1
500	fcc	5 × 5 × 5	3 × 3 × 3	0.05
1372	fcc	7 × 7 × 7	2 × 2 × 2	0.05

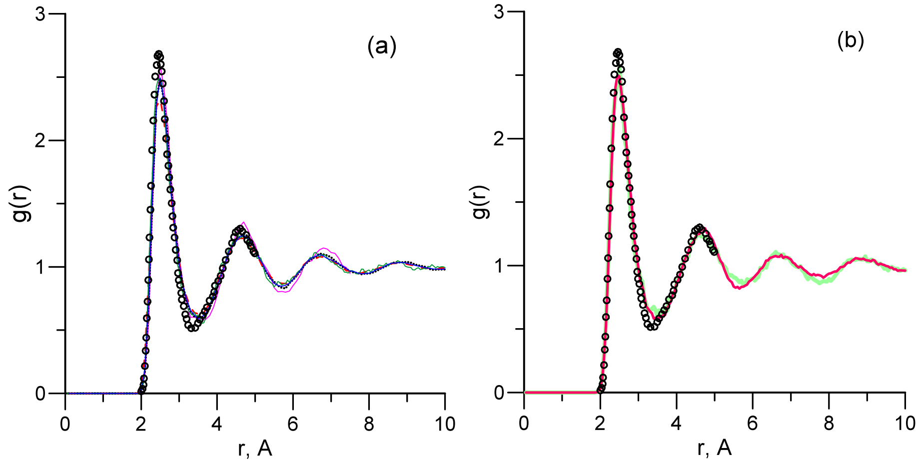

Fig. 3. Pair-correlation function of copper at density of 8 g/cm^3 and temperature of 2000 in the computational cells with different shapes and initial atomic distributions. *a*: The results obtained for the cubic cells in comparison with the experimental data [59] obtained at temperature of 1398 K. *b*: The results obtained for the cells with different sides are compared with the same work.

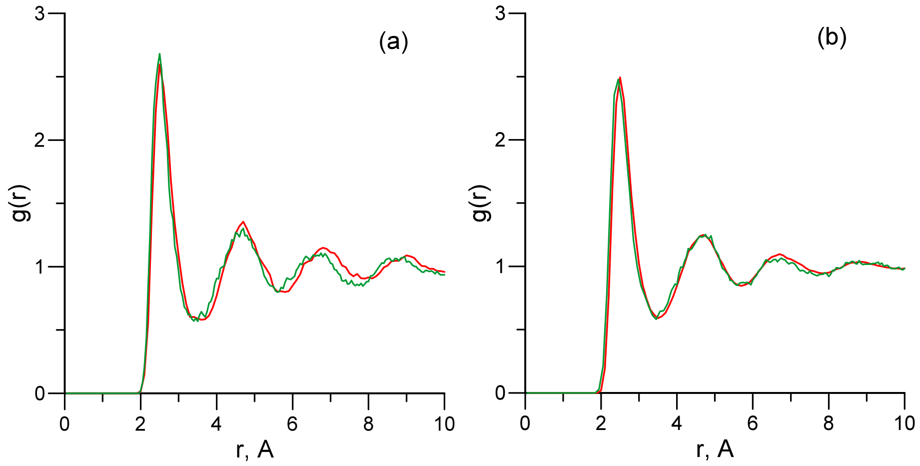

Fig. 4. Pair-correlation functions of copper at density of 8 g/cm^3 and temperature of 2000 K for the computational cells where the number of atoms is the same or slightly different. *a*: The results obtained for the cubic (red line) and elongated (green line) computational cells with 108 and 112 atoms, respectively. *b*: The comparison of the results corresponding to the cubic (red line) and planar (green line) cells. Both cells contain 216 atoms.

Considering these data, we can independence of PCF‘s on the cell shape form, because of other parameters of these calculations were the same. In Fig. 4 (a), we can see two curves are appreciably different, whereas in the right figure an agreement was reached. Therefore, we can use non-cubic computational cells with no restrictions if the number of atoms is enough for satisfactory convergence with this parameter.

The discussion of the results obtained by our calculations based on the Kubo-Greenwood formula for the heat conductivity and the electric resistivity starts with the check of convergence for cubic cells. As shown in the Fig. 5 (a), heat conductivity obtained for the cubic cells increases with the number of particles in the cell. The type of an initial lattice, from which the simulation process began, is marked for each point. No differences between the data corresponding to the cells with initial fcc, bcc, and sc arrangement of atoms are found that can overcome a level of the calculation error. Red dashed line corresponds to the approximation of the form:

$$\hat{\kappa}(N_{at}) = \frac{180.7}{1.088 + 168.9/N_{part}^{4/3}}. \tag{2}$$

Similar behavior is observed at the Fig. 5 (b) for the electric

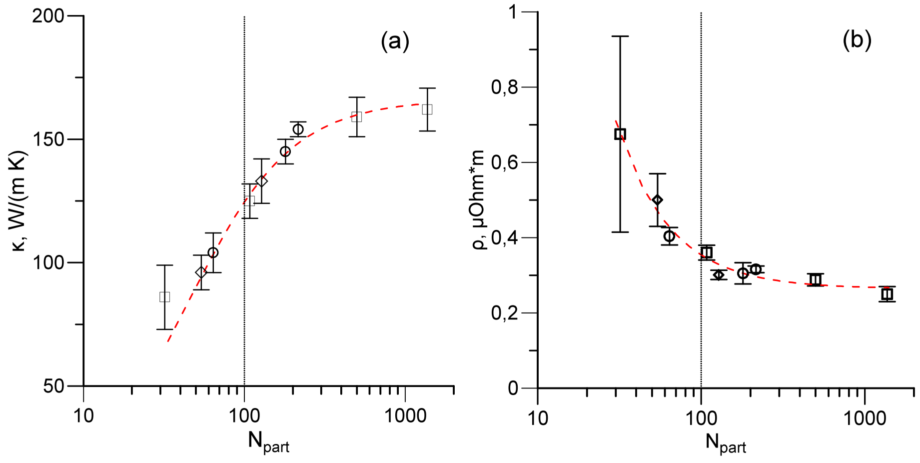

Fig. 5. Check of convergence with a number of atoms for copper at density of 8 g/cm^3 and temperature of 2000 K. *a*: Heat conductivity calculated for the cells with cubic shape: (squares — fcc, diamonds — bcc, circles — sc). The fit of the calculation data (Eq. (2)) is shown by the red dashed line. The results calculated previously [21,56] are represented to the left from the vertical dashed line. *b*: Electrical resistivity of copper at the conditions called above. Fit Eq. (3) are shown by the red dashed line.

resistivity of copper. The explicit form of the approximation for electric resistivity as a function of the cell size is written as:

$$\hat{\rho}(N_{at}) = \frac{41.52}{N_{part}^{4/3}} + 0.269 \tag{3}$$

We can note that the functional form and the degree for the number of particles N_{part} in the formulas (2) and (3) were previously assumed instead of adjustment by the method of least squares as the other coefficients. Their determination in the expression (3) can be carried out using the well-known Ziman [60] formula by way of estimation of an error occurs due to the clipping of the pair-correlation function at large scales. It should be assumed that on a narrow range of wave vectors q, determined from zero to $2\pi/a$, where a is the size of the cube side, an error of structural factor obtained from the pair-correlation function does not depend on q.

The expression (2) is obtained from the formula (3) by the use of the Wiedemann-Franz law. In the work [21], the authors found that in copper this law is performed for the different electron and ion temperatures.

The result of extrapolation of the experimental data [61] for copper on a binodal curve at a temperature of 2000 K, which corresponds to a density of 7.5 g/ cm^3, gives a heat conductivity of 171 W/m/K, whereas our result for the cell with 1327 atoms — 162 W/m/K. The electric resistivity obtained for this point at the binodal measured in another experiment [58] is almost the same as our result. This experiment gives 0.26 μOhm*m [58], while according to the results of the convergence test we have in the limit of large cells 0.25 μOhm*m.

In the error bars shown in Fig. 5, we have taken into account the error due to a finite number of atoms, the density of the k-grid, and the smearing of the Gaussian function. Effects of other parameters on the transport properties, such as the cutoff energy and the number of empty electron states, was found to be noticeably less than those listed above.

If we consider the data for the heat conductivity obtained in the cells of non-cubic form, it is possible to prove the insensibility of the results to the cell shape. For Fig. 6 (a), there are shown behavior of the diagonal components of the heat conductivity tensor $\kappa_>$ and $\kappa_<$ corresponding to the directions of the longest ($l_>$) and shortest ($l_<$) sides of the cell. The first, as expected, is more than the second in all cases. However, their difference has a value close to the calculation error. In addition to the calculated components of the heat conductivity tensor in Fig. 6 (a) the lines corresponding to the assumption that $\kappa_>$ depends only on $l_<$ are also demonstrated. Here, we consider a cube with a side is equal to the largest side of a non-cubic cell and find the number of atoms in such a cube at the considered material density. Then, we use the expression (2) to estimate a heat conductivity corresponding to such a cube. The same process we provide for the smallest side of a non-cubic cell. Due to Fig. 6 (a), the line corresponding to the largest side comes hardly to the error bars of the calculated $\kappa_>$. On the contrary, the similar estimation for $\kappa_<$ is two times lower than those obtained in the direct calculation. The proximity of the calculated and assumed values in the case of the largest side is explained by the fact that the expression (2) assumes fast convergence with the cell size. Therefore, it would be incorrect to assume that the calculated values $\kappa_>$ and $\kappa_<$ depend only on the cell side length.

The approximation (2) presented in Fig. 6 (a) are restricted by the data for $\kappa_>$ and $\kappa_<$.

However, we can show there is no even more general dependence on the shape of the cell if the number of atoms is constant. Suppose that the opposite is true, and the $\kappa_>$ is some function $\phi(l_>, l_<)$. The functional form of such a function does not coincide necessarily with the form of the formula (2). For symmetry reasons, the function corresponding to the smaller component should differ only in the order of variables: $\phi(l_<, l_>)$. Denote the ratio $l_>/l_<$ as ϵ, and enter the following value:

$$\delta = \frac{(\kappa_</l_<)}{(\kappa_>/l_>)}. \tag{4}$$

In Fig. 6 (b), the dependence of Eq. (4) on ϵ is presented. It is evident that the straight line fitting this dependence is proportional to ϵ with good accuracy. Therefore, we can conclude that the ratio of $\kappa_>/\kappa_<$ does not depend on ϵ. Thus, if we substitute the variables of ϕ from $l_>, l_<$ to their product and quotient, which is one-to-one mapping for any non-zero and, of course, positive $l_>$ and $l_<$, then we will only obtain the dependence on the product of the two original variables. Taking into account that the third side of our cell always coincides with a one of the other two, we realize that only the dependence on the volume should be preserved or, equivalently, on the number of particles.

Thus, according to the calculation results and the provided analysis, the change in the aspect ratio of the cell sides at the fixed number of atoms has no any effect on the convergence in size of the cell.

The main conclusions of this section are the independence of the process of convergence in the number of particles on the initial distribution of atoms, at least if it corresponds to cubic symmetry and cell shape. Convergence in the number of particles is achieved for liquid copper at a temperature and density that is near the binodal, and for a number of atoms not less than 200. With the value of 128 atoms in a cell used in further calculations of noble metals, the convergence error due to a finite cell size should be estimated at 25%. We also note that the maximum of heat conductivity according to the formula (2) is close to

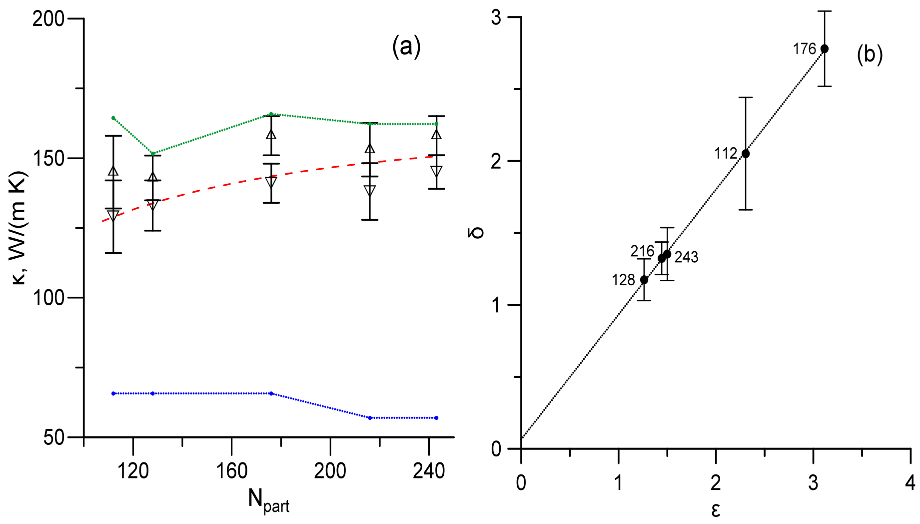

Fig. 6. Diagonal components of heat conductivity tensor for copper at density of 8 g/cm^3 and temperature of 2000 K in the case of the cells with a non-cubic shape. *a*: The results for the components corresponding to the long and short sides of computational cells are shown by up and down triangles. Red dashed line represents the approximation Eq. (2) which one was derived using the data for the cubic cells. Green dashed line are used for the data of usage of the approximation Eq. (2) for a number of atoms in the cube with the side is equal to the long side of a computational cell. Similarly, the blue dashed line represents an estimation obtained for a number of atoms in the cube with the side is equal to the short side of a computational cell. *b*: Dimensionless parameter δ as a function of the ratio between the long and short sides of a computational cell. The black line represents a curve obtained from the calculated results using the least square method.

the result [56], obtained in the all-electron approach for a fcc cell with 108 atoms that was equal to 180 W/m/K.

2.4. Hybrid functionals in the case of Si

In the paper [51] dedicated to the properties of liquid and amorphous silicon, it is discussed that the transition from a state with covalent bonds between atoms to a state with metal bonds occurs gradually with increasing temperature. Determination of the electron density distribution depends to a considerable degree on the description of the exchange and correlation interaction between electrons. According to Ref. [51], usage of the hybrid SCAN [62,63] functional allows to obtain the melting point closer to the experimental value (1685 K, [64]) than by use of the generalized gradient approximation. Further, considering the transport properties of silicon, we also apply some hybrid functionals [65-68] to consider their effect.

In this approach, the change of the electron density in the exchange-correlation functional is evaluated by means of gradient corrections. This approximation can lead to an inaccurate description of the electron density distribution if valence electrons redistribute more localized than in metals.

Two tests were conducted to answer these questions. In the first one, we considered silicon at temperature of 3500 K, where the transition to the liquid metal state is supposed to be complete. In this case, calculations are also carried out for the cells of a larger size (128 and 256 atoms). The results of these calculations are given in Table 3.

According to Table 3, the convergence of the transport properties is achieved for silicon if the computational cell contains 128 atoms.

A second test consisted of the use of hybrid functionals at the stage of calculation of one-electron wave functions and energies. Here, the cell size was the limiting factor, which is why such a small cell was used in the calculations of silicon properties mentioned above. In addition to the PBE exchange-correlation functional [42], other functionals [65,66] and [67,68] were also used. If the choice of the first of them can be explained due to its popularity between the other hybrid functionals, the second is known as a reproducing one of experimental data for the band gap [69]. Recently, the possibility to use this functional in the case of the transport properties calculation of aluminum has been successfully demonstrated in a wide area of the phase diagram corresponding to the warm dense matter [70]. Using these functionals, we calculated transport properties of the silicon at temperature of 1700 K to reveal importance of the exchange-correlation functional for the Kubo-Greenwood calculations. The results of this test are presented in Table 4.

According to Table 4 the hybrid HSE functional lies between the results of the other functionals we used. In the sense of agreement with experiment, the data obtained using this functional are in good agreement. On the other hand, authors noted previously [21] that there is no dependence was found for the heat conductivity of copper whether the local density approximation [73] or the generalized gradient approximation [42] are used to describe the exchange-correlation interaction.

Table 3
The electric resistivity and heat conductivity of molten silicon at the temperature of 3500 K and different computational cell sizes.

Number of atoms	ρ, μOhm*m	κ, W/(m K)
64	0.72(0.17)	123(33)
128	0.78(0.15)	119(33)
256	0.77(0.16)	116(33)

Table 4
The electric resistivity and heat conductivity of molten silicon at temperature of 1700 K and the different methods of calculation in comparison with the experimental data.

xc-functional/ number of atoms	ρ, μOhm*m	κ, W/(m K)
PBE, 64 atoms	0.5(0.2)	98(32)
PBE, 128 atoms	0.49 (0.15)	97(31)
B3LYP, 64 atoms	1.9(0.5)	41(11)
B3LYP, 128 atoms	1.6(0.3)	42(14)
HSE, 64 atoms	0.8(0.2)	60(17)
Experiment	0.73 [64]	51.5 [71]; 58.6 [72]

3. Results

3.1. Frequency of the electron-electron collisions in the Kubo-Greenwood calculations

In our previous works [21,56], the question was raised as to how complete description of electron-electron interaction in density functional calculations of transport properties based on the Kubo-Greenwood formula if this type of interaction implied here in the exchange-correlation functionals [73,42]. As we know, these functionals were developed for electron gas at zero temperature, and their applicability is a subject of some recent theoretical investigations [74,75]. As was noted for copper on isochore of 8 g/cm^3 and electron temperatures from 2000 to 55, 000 K [21,56], the results corresponding to these functionals give almost the same result. Comparison with the analytical model [56] for solid and liquid copper in a two-temperature state was considered as a reason to conclude electron-electron collisions are lacked at this calculation. Also, the idea of adding the contribution of electron-electron collisions, obtained by our semianalytical model [76] was discussed.

In order to obtain a clearer perception of this problem, we carried out a series of calculations of the heat conductivity by the Kubo-Greenwood formula for thermodynamic states with various electron and ion temperatures. The significant difference between the two temperatures was used in order to distinguish the effects of an electron and ion heating. There were considered atomic configurations with 32, 64, and 128 atoms. The data for heat conductivity and electric resistivity in this way made it possible to verify the convergence with the cell size behaves the similar to the case discussed in detail in the previous section.

Data on the number of valence s-band electrons z_s, their effective mass m_s, partial heat capacity C_s and mean square velocity V_s^2 were used from the model [76]. Its data for electron-electron collision frequencies (ν_{ss} and ν_{sd}) were also used. As for electron-ion collision frequency, we used the Drude analysis of the Kubo-Greenwood calculation results for electric resistivity ρ instead of the fit constructed by extrapolation of experimental data with the maximum value in the Ioffe-Regel model:

$$\nu_{si} + \nu_{sd} = \frac{e^2 n_s \rho}{m_s}. \tag{5}$$

Here, n_s is the volume concentration of s-band electrons, and m_s is the effective mass of the s-electron evaluated in the two-parabolic approximation [76].

Using this expression, we assume the following conditions. First, we suppose that in copper the transfer of charge and energy occurs mainly due to s-band electrons. According to the estimates made in the relaxation-time approximation [76], the d-band electron contribution to the electric conductivity is much less than the s-band electron contribution. Secondly, we assume that the *umklapp* processes in electron-electron collisions are too weak to take into account their contribution. Otherwise, we would add this contribution to the left side of the expression (5).

The assumption was made that the frequency of electron-electron collisions depends only on the electron temperature, and the frequency of electron-ion collisions is only determined by ion temperature.

$$\nu_{si}(T_i) + \nu_{sd}(T_e) = \frac{e^2 n_s \rho}{m_s}. \tag{6}$$

The latter part of the previous statement is confirmed by the results of Ref. [31] for aluminum, where the electric resistivity obtained using the Kubo-Greenwood formula was revealed as constant if only the electron temperature changed. Since aluminum has one valence band, the frequency of electron-ion collisions in it corresponds fully to the right part of the expression (5). As for the independence of the electron-electron collision frequency on the ion temperature, here we rely on the fact that in the semianalytical approach we used [33,76], the effective frequency is determined in the relaxation-time approximation by the quantities depending only on the electron temperature. According to the model of two-temperature electron structure of copper [76], we use the number of s-electrons per atom is equal to 1, and the effective mass for electrons of this band is equal to 0.77 electron mass in vacuum.

A separation of the contribution of electron $s-d$ collisions was provided directly from the Kubo-Greenwood calculations using Eq. (6). For this aim, the grid of ion and electron temperatures was chosen so as to have a series of calculations, where we can neglect by the contributions of electron-electron collisions due to small electron temperature. In the second series, we increase only electron temperature and can exclude electron-ion contribution for fixed small ion temperature which we have known on the previous step. At the third step, one-temperature heating was considered, during which the frequency of electron-ion collisions increases slowly, while the total frequency of electron-electron collisions becomes at $T = 15{,}000$ K the same order of magnitude as ν_{si}. Due to this procedure, we can compare the result based on the first-principles calculations with the data of the semianalytical approach for both the one-temperature and two-temperature heating (see Table 5).

Here, we should remind that Kubo-Greenwood calculation technique as it implemented in many DFT computational packages [43,77,78] implies an application of the random-phase approximation (RPA) in the initial expression for the flux-flux correlation function [79]. Formally, we have no any intraband contribution using the RPA [80]. In the work [81], the simple method was introduced which one makes possible to include this contribution. Here, the linearization of band dispersion and the time-dependent density functional theory (TDDFT) are used. On the other hand, the approach [81] requires a usage of phenomenological estimations for the coefficient which is responsible for the mean quasiparticle lifetime. We can suggest another simple method to take this contribution into account in the static limit for electric and heat conductivity where phenomenological assumptions are also used.

Table 5

Electric resistivity and effective frequencies of electron collisions for copper at different ion and electron temperatures (in K). The electric resistivity (in μOhm*m) calculated using the Kubo-Greenwood formula. The frequencies ν_{si}^{KG} and ν_{sd}^{KG} in the fourth and fifth column are the results of the separation procedure provided with the use of the expression (6) and the data from the third column. Here, we use the parameters of electronic structure n_s and m_s published in Ref. [76] and the effective frequencies of the electron-ion and electron-electron collisions for copper in one- and two-temperature states. The effective frequencies of $s-d$ and $s-s$ electron-electron collisions obtained by the use of semianalytical approach based on relaxation-time approximation [33] with the same parameters for n_s and m_s as given in Ref. [76] are shown in the sixth and seventh columns. All data for frequencies are given in fs^{-1}.

T_e	T_i	ρ_{KG}	ν_{si}^{KG}	ν_{sd}^{KG}	ν_{sd}^{2p}	ν_{ss}^{2p}
2000	2000	0.31(± 0.02)	0.83(± 0.05)	0(0)	0.00001	0.02
7500	7500	0.52(± 0.02)	1.08(± 0.10)	0.30(0.10)	0.36	0.37
15,000	15,000	0.53(± 0.02)	1.23(± 0.15)	0.19(0.15)	1.97	1.44
20,000	2000	0.39(± 0.02)	0.83(± 0.10)	0.22(0.10)	2.70	2.22
30,000	2000	0.54(± 0.02)	0.83(± 0.05)	0.62(0.10)	3.38	3.65
2000	7500	0.4(± 0.02)	1.07(± 0.05)	0(0)	0.00001	0.02
2000	15,000	0.46(± 0.04)	1.23(± 0.10)	0(0)	0.00001	0.02

Further, we will use the other Drude relation for heat conductivity:

$$\varkappa_D = \frac{C_s V_s^2}{3(\nu_{si} + \nu_{sd} + \{\nu_{ss}\})}. \tag{7}$$

Here, C_s is the volume heat conductivity of s-band electrons, V_s^2 is the mean square velocity of s-band electrons. This parameters as well as one used in the expression (5) are brought from the work [76]. We should emphasize that such an analysis based on the expression (7) implies that s-band and d-band electrons have the same temperature. As was recently demonstrated by the use of TDDFT calculations [82], instantly excited s-band and d-band electrons are in the states of mutual equilibrium at the timescale of about 10 attoseconds.

To establish the role of electron-electron collisions in heat conductivity, the following hypotheses were proposed to investigate possible variants of describing electron-electron collisions. The first one consists in neglecting electron $s-s$ collisions: the frequency in the expression (5) coincides with the total frequency in the denominator of the expression (7):

$$\varkappa_1 = \frac{C_s V_s^2}{3(\nu_{si}^{KG} + \nu_{sd}^{KG})}. \tag{8}$$

The second hypothesis assumes that the contribution of the electron $s-d$ collisions obtained in the semianalytic approach [76] must be used in the expression (7) instead of ν_{sd}^{KG} as it was in the previous expression:

$$\varkappa_2 = \frac{C_s V_s^2}{3(\nu_{si}^{KG} + \nu_{sd}^{2p})}. \tag{9}$$

In the third case, we added the intraband contribution of electron-ion collisions ν_{ss}^{2p} to the frequencies obtained in the first-principles calculation by the use of the Drude formula (6):

$$\varkappa_3 = \frac{C_s V_s^2}{3(\nu_{si}^{KG} + \nu_{sd}^{KG} + \nu_{ss}^{2p})}. \tag{10}$$

The fourth hypothesis is similar to the previous but all the electron-electron contributions are obtained in the semianalytical approach:

$$\varkappa_4 = \frac{C_s V_s^2}{3(\nu_{si}^{KG} + \nu_{sd}^{2p} + \nu_{ss}^{2p})}. \tag{11}$$

The resulting heat conductivities according to the above four hypotheses are collected in Table 6. Observing the data for the first hypothesis we can note immediately the assumption, that there are lack of any electron-electron contributions in the Kubo-Greenwood approach, should be discarded. In the case when the electron temperature becomes more than 10, 000 K, the effect of electron-electron collisions is already large enough and must be taken into account correctly. At high electron temperatures, the data of only second and third hypotheses are close to the Kubo-Greenwood calculation results. We can note the result of the fourth hypothesis is noticeable smaller than one have calculated by the Kubo-Greenwood formula.

As was mentioned above, the fourth hypothesis is the most close to the semianalytical approach we used [76]. Thus, we can conclude that the use of this approach leads to an overestimation of the electron collision frequency used in the denominator of the expression (7). The values of the semianalytical result for ν_{sd} are close to the sum of the other seminanalytical result for ν_{ss} and the data of first-principles calculations for ν_{sd} obtained by the use of the Drude formula (6). It is a consequence of more steep growth of ν_{sd} with electron temperature in comparison with the behavior of ν_{ss} at the same conditions [33].

Using these facts, we can suppose the reason of difference between the data of the fourth hypothesis and the Kubo-Greenwood calculation is the interband contribution ν_{sd}^{2p} included in the former case. Thus,

Table 6
The comparison of the hypotheses based on the Drude formula (7) for the heat conductivity of copper (in W/(m*K)) at density of 8 g/cm^3 with the first-principles data. The results corresponding to the formulas (8)–(11) are shown in the third, fourth, fifth, and sixth columns, respectively. Such characteristics of s-band electrons in copper as partial heat conductivity C_s and mean square velocity V_s^2 are brought from the work [76]. All temperatures are given in Kelvins.

T_e	T_i	κ_1	κ_2	κ_3	κ_4	κ_{KG}
2000	2000	168(± 12)	168(± 12)	164(± 12)	164(± 12)	141(± 48)
7500	7500	543(± 21)	527(± 12)	432(± 12)	422(± 16)	307(± 104)
15,000	15,000	1617(± 60)	719(± 23)	804(± 12)	496(± 12)	531(± 185)
20,000	2000	3255(± 163)	967(± 29)	1043(± 12)	593(± 12)	1103(± 385)
30,000	2000	3944(± 144)	1361(± 22)	1123(± 12)	729(± 12)	1682(± 668)
2000	7500	130(± 7)	130(± 7)	128(± 12)	128(± 12)	109(± 37)
2000	15,000	113(± 11)	113(± 11)	111(± 12)	111(± 12)	97(± 33)

reliability of the semianalytical data for the interband contribution is an open question. The similar conclusion can also be given for the intraband contribution calculated in the RTA approach. If we look to the results of the third hypothesis and assume that the data of $s - s$ collision frequency is correct, we would arrive to the contradictory conclusion about a role of intraband contribution to the results of the Kubo-Greenwood calculations. Thus, both the results of semianalytical approach should pass through a revision.

Finally, the results of the Kubo-Greenwood calculation analyzed by the Drude model shows internal consistency: the difference in the frequency of electron collisions, the corresponding heat conductivity and electric resistivity in the Drude model, are in mutual compatibility. Taking into account the accuracy of the performed calculations, we also may say that our results obey the Wiedemann-Franz law.

3.2. Two-temperature heat conductivity at a fixed volume

According to the results of the calculations based on the Kubo-Greenwood formula [30] and also to the analytical models [33], the electron heat conductivity of noble metals in the two-temperature state differs significantly from its value under normal volume. This fact should be taken into account when two-temperature hydrodynamic calculations are carried out. The analysis provided for copper shows that the results presented earlier [21] may not be accurate enough, and they should be compared with the results of this work.

Heat conductivity, as shown in Fig. 7 (a), according to the data obtained in this work, tends to grow linearly with electron temperature. The results of the previous studies provide lower values, which are to be expected as a consequence of monotonically increasing heat conductivity with the number of atoms in the computational cell. In comparison with the data of extrapolation of the experiment [61], the calculation carried out in this work on a larger cell is closer to it, although there is no such noticeable difference as in Fig. 8 (b). In contrast to the results for electric resistivity, the heat conductivity calculated by the PAW method in the case of the 32-atom cell has the same slope as in the new calculation. At the same time, all-electron calculation [56] gives a slower increase in the electron conductivity with the increase of electron temperature.

In Fig. 7 (b), there are shown the calculation carried out in the PAW-approach for 128 atoms is closer to the experimental data [58] and demonstrates qualitatively correct behavior in comparison with the previous data. This note relates to the results of Refs.[21,56], which was also obtained using the PAW method but differed mainly by the noticeably smaller cell size (32 atoms). The results of the full-electron approach obtained in the work [21] with the same cell, are closer to the present data and characterized by a sharper growth with electron temperature.

The data obtained for gold, presented in Figs. 8 and 9 are gathered in such a way to have a perception of significance of the effect of compression from density of 17 g/ cm^3, which corresponds to the equilibrium at 2000 K, up to 19.3 g/ cm^3. The differences caused by the compression are of the same order with the error of calculation for both electric resistivity and heat conductivity.

We can also note by comparing the left and right parts of Figs. 8 and 9, that the difference of these results is only in the way of preparation of atomic configurations for the direct calculation of the transport properties and it disappears with the increase of electron temperature. At low temperatures, it is quite noticeable even in comparison with the effect of compression discussed above.

A linear increase in the heat conductivity occurs in this interval of electron temperature. In Ref. [30], the same behavior was observed for the thermal conductivity of solid gold with hot electrons and at density of 19.32 g/ cm^3.

3.3. Heat conductivity of molten metals at atmospheric pressure

Leaving behind the demands appropriated to the description of the irradiation by femtosecond laser pulses, to the results that are necessary to describe the processes inherent to the relaxation after nanosecond laser exposure, we define firstly what we will further consider as the

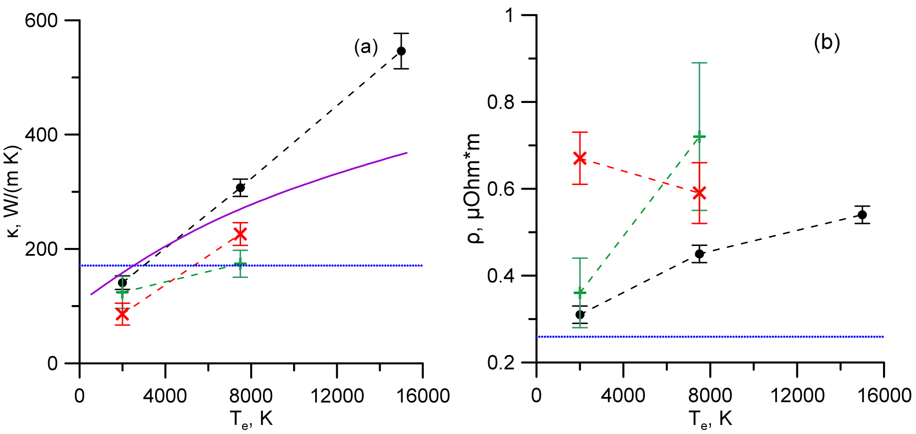

Fig. 7. Transport properties of copper (ρ = 8 g/cm^3, T = 2000 K) in a two-temperature state in comparison with the data of our previous works. *a*: Heat conductivity. Extrapolation [61] of the experimental data corresponding to temperature of 1756 K are shown by the blue line. The results of the semi-analytical model of electron transport presented in Ref. [56] are shown by the purple line. *b*: Electric resistivity. New data are shown by black points. Red and green points correspond to the PAW and full-potential calculations [21,56]. The blue line represents the experimental data [58] measured for the same density and temperature of 1988 K.

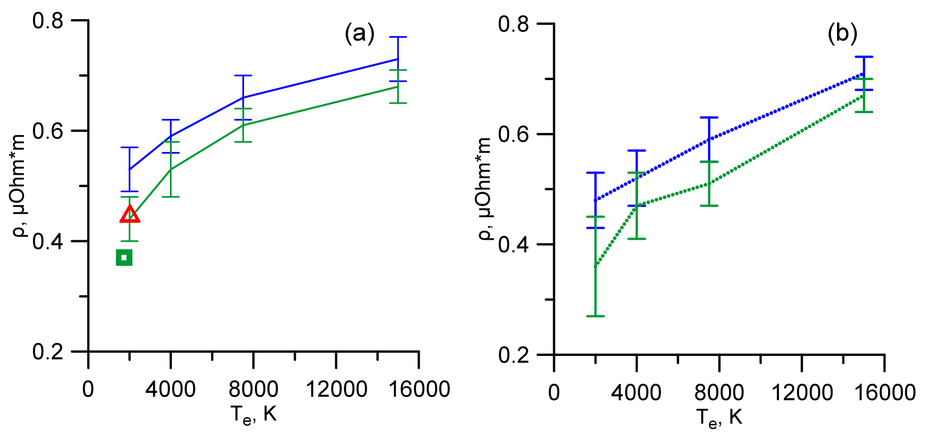

Fig. 8. The electric resistivity of gold in two-temperature state at densities of 17 and 19.3 g/cm^3 and ion temperature of 2000 K (blue and green lines). *a*: The results corresponded to atomic configurations from QMD calculations. The experimental data of Ref. [58] corresponding to a temperature of 2024 K are shown by the open red triangle and the other experimental result [83] was obtained for temperature of 1737 K are shown by open green square. *b*: The results obtained using classical MD simulations where the interatomic potential in EAM parametrization [54] was used.

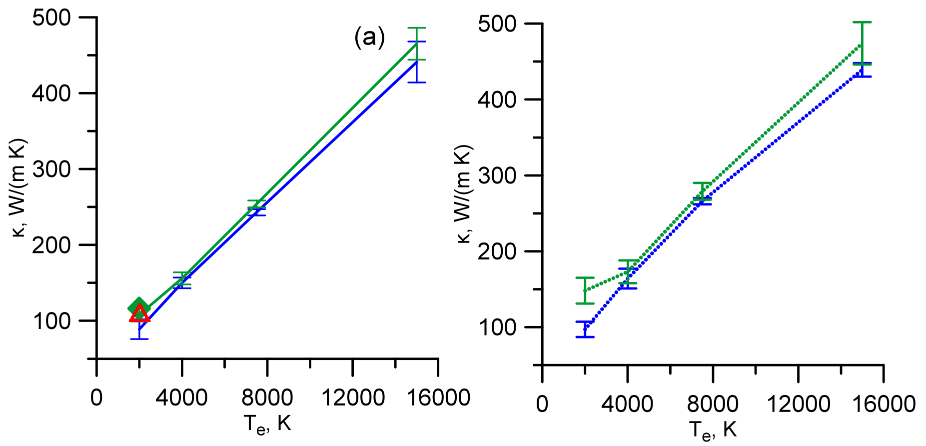

Fig. 9. Heat conductivity of gold in two-temperature state at densities of 17 and 19.3 g/cm^3 and the ion temperature of 2000 K (blue and green lines). *a*: The results of the QMD calculations. The result of extrapolation of experimental data provided by Ref. [58] corresponding to a temperature of 2024 K are shown by the open red triangle while the other point [83] are evaluated using the Wiedemann-Franz law are represented by the open green square. *b*: The results of the classical MD simulations provided by the use of the EAM potential [54].

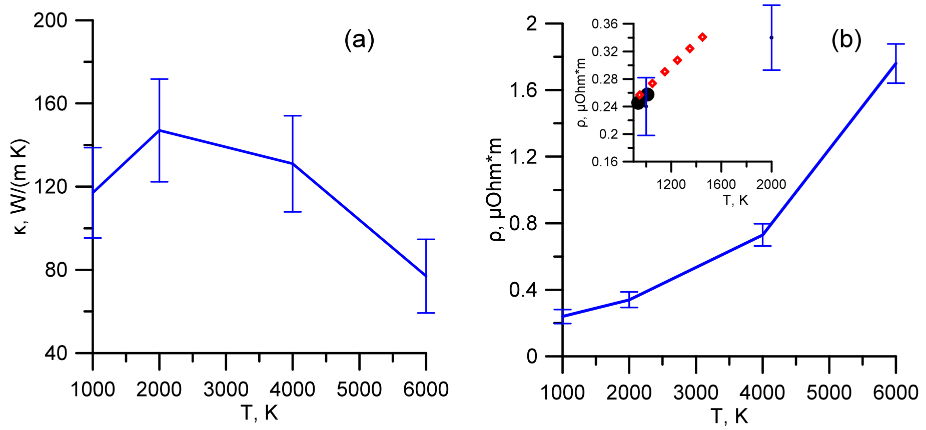

Fig. 10. Heat conductivity (*a*) and electric resistivity (*b*) of molten aluminum at an isobaric expansion. Comparison with the experiments [84,85] represented by the black circles and the red diamonds are given in the inset.

equilibrium density. Here we are talking about the temperature-dependent density of the liquid metal, which is the equilibrium at atmospheric pressure. For aluminum and copper, the data of wide-range equations of state were used [86]. Experimental data [58,87,64] were used for titanium and silicon.

The results of the calculations for the group of three metals and liquid silicon are presented below. Since these calculations relied on a fixed heating pressure rather than volume, this makes it possible to conduct a more detailed comparison with the experimental data than it was done for isochoric heating.

Comparing the results of Figs. 10 and 11, obtained for aluminum and copper melts, we can note that, within the accuracy which is proper to the heat conductivity calculation, its behavior at isobaric expansion can be considered as independent on temperature. At the same time, there is a monotonous increase in the electric resistivity. At the temperatures where the comparison was made with the data of the experiments for aluminum [84,85] and copper [58], they have satisfactory agreement with the results for electric resistivity.

As shown in Fig. 12 for the case of molten titanium, behavior of the heat conductivity and the electric resistivity are opposite to those observed previously in Figs. 10 and 11. We can explain this fact as a consequence of one of the largest electric resistivity of the pure metals achieved with the heating [58]. The growth of heat conductivity occurs in accordance with the Wiedemann-Franz law $\kappa \sim T\rho^{-1}$. The

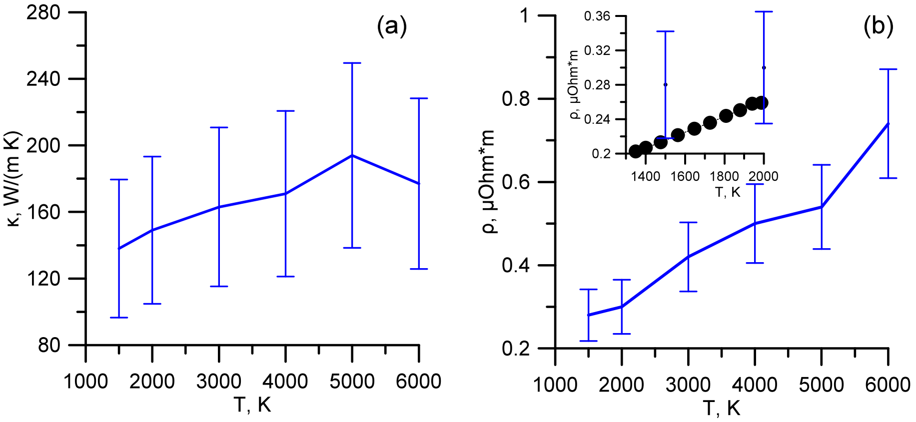

Fig. 11. Heat conductivity (*a*) and electric resistivity (*b*) of molten copper at an isobaric expasion. Comparison with the experimental data [58] is shown in the inset.

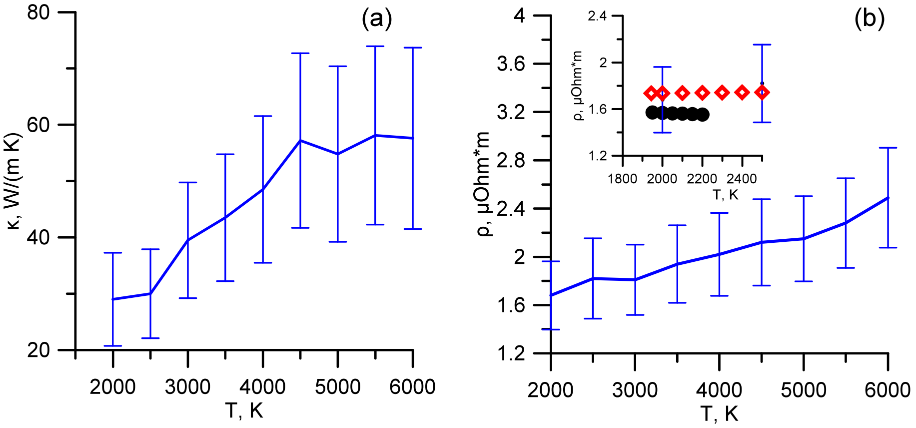

Fig. 12. Heat conductivity (*a*) and electric resistivity (*b*) of molten titanium at an isobaric expansion. The data of the experiments [87,58] are shown in the inset by the black circles and the red diamonds.

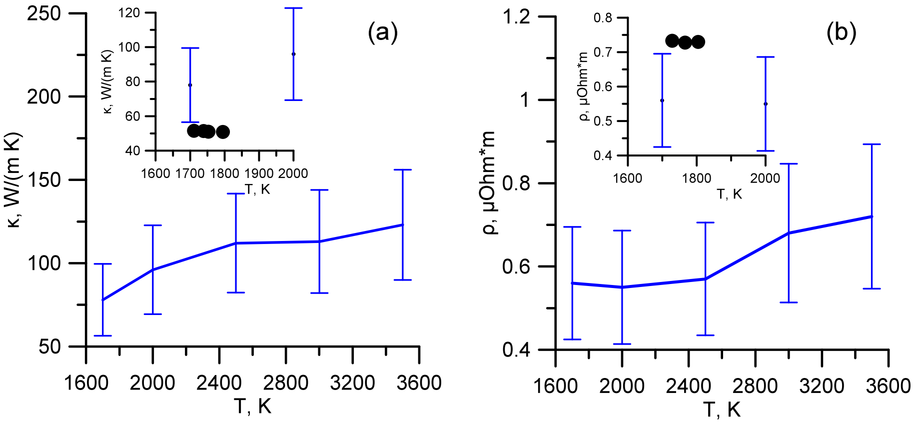

Fig. 13. Heat conductivity (*a*) and electric resistivity (*b*) of molten silicon at an isobaric expansion. The experimental results for heat conductivity [71] and electric resistivity [64] are represented in the inset.

corresponding coefficient in this law for liquid titanium is close to the ideal value (2.44 10^{-8} W*Ohm /K^2) in the entire temperature range we considered.

In the case of silicon, a moderate increase in heat conductivity is observed (see Fig. 13), while the electric resistivity can be considered constant within the accuracy of the calculation. We should note that agreement with the experimental data for the melting point is not observed. This issue can be caused by the insufficiency of the cell size (64 atoms) or by an improper description of the exchange-correlation interaction [42], which is proven to be suitable for metals. For a substance near the transition from a semiconductor to metal, this approach should be checked in detail. Using the data of the test we described in the last part of Section 2, we can suppose, that usage of HSE [67,68] hybrid functional for silicon can provide better accuracy of the Kubo-Greenwood calculations of electrical resistivity and heat conductivity.

4. Conclusions

The analysis of possible improvements of the calculation scheme used to obtain transport properties of liquid metals is carried out. Proposals were considered to extend the possible initial configurations, to select non-cubic cells for the calculation of electric and heat conductivity tensors, and to apply the classical molecular dynamics method to obtain atomic configurations. It was checked that the first and third proposals can be considered as successful.

The cell size convergence of the heat conductivity of liquid copper is investigated. It is shown that the convergence with the cell size is achieved if the last one contains at least 200 atoms.

The role of electron-electron collisions in our calculations based on the Kubo-Greenwood formula is analyzed. Comparison with the data of semianalytical model based on a simplified electron dispersion law and relaxation-time approximation, which was developed for calculations of partial frequencies of electron collisions, reveals the results obtained by the use of the Kubo-Greenwood formula differs significantly from the data of the semianalytical calculations in the case of collision frequency of interband electrons. At this time, the semianalytical data for heat conductivity demonstrate more slow increase with electron temperature than the results of Kubo-Greenwood calculation. It agrees with the exclusion of intraband contribution to transport properties implied in the density-functional calculations based on the Kubo-Greenwood formula.

The behavior of heat conductivity and electric resistivity of copper and gold in a two-temperature state and isochoric heating was found insensible to the used method of melting. The data for the electric resistivity of aluminum, copper, titanium, and silicon at constant pressure were detected in good agreement with the experimental results. In the case of silicon, the essential role of the used exchange-correlation functional was demonstrated.

Acknowledgments

This work was supported by Russian Foundation for Basic Research (grant No. 16-20-00864).

References

[1] A.Y. Vorobyev, V.S. Makin, C. Guo, Periodic ordering of random surface nanostructures induced by femtosecond laser pulses on metals, J. Appl. Phys. 101 (2007), https://doi.org/10.1063/1.2432288 034903–(1-5).

[2] G. Norman, S. Starikov, V. Stegailov, V. Fortov, I. Skobelev, Nanomodification of gold surface by picosecond soft X-ray laser pulse, J. Appl. Phys. 112 (2012), https://doi.org/10.1063/1.4731752 013104–(1-8).

[3] Y. Nakata, N. Miyanaga, K. Momoo, T. Hiromoto, Solid-liquid-solid process for forming free-standing gold nanowhisker superlattice by interfering femtosecond laser irradiation, Appl. Surf. Sci. 274 (2013) 27–32, https://doi.org/10.1016/j.apsusc.2013.02.042.

[4] A. Kuchmizhak, S. Gurbatov, A. Nepomniaschiy, A. Mayor, Y. Kulchin, O. Vitrik, S. Makarov, S. Kudryashov, A. Ionin, Hydrodynamic instabilities of thin Au/Pd alloy film induced by tightly focused femtosecond laser pulses, Appl. Surf. Sci. 337 (2015) 224–229, https://doi.org/10.1016/j.apsusc.2015.02.098.

[5] T.-H. Her, R.J. Finlay, C. Wu, S. Deliwala, E. Mazur, Microstructuring of silicon with femtosecond laser pulses, Appl. Phys. Lett. 73 (1998) 1673–1675, https://doi.org/10.1063/1.22241.

[6] J. Eizenkop, I. Avrutsky, G. Auner, Single pulse excimer laser nanostructuring of thin silicon films: nanosharp cones formation and a heat transfer problem, J. Appl. Phys. 101 (2007), https://doi.org/10.1063/1.2720185 094301–(1-7).

[7] M. Gedvilas, S. Indrisiunas, B. Voisiat, E. Stankevicius, A. Selskis, G. Raciukaitis, Nanoscale thermal diffusion during the laser interference ablation using femto-, pico-, and nanosecond pulses in silicon, Phys. Chem. Chem. Phys. 20 (2018) 12166–12174, https://doi.org/10.1039/C7CP08458G.

[8] S. Gurbatov, O. Vitrik, Y. Kulchin, A. Kuchmizhak, Mapping the refractive index with single plasmonic nanoantenna, Sci. Rep. 8 (2018), https://doi.org/10.1038/s41598-018-21395-w 3861–(1-9).

[9] E.S. Wyndham, M. Favre, H. Chuaqui, P. Choi, A.M. Lenero, J.S. Diaz, Reproducibility of a titanium plasma vacuum spark discharge, IEEE Trans. Plasma Sci. 33 (2005) 1662–1667, https://doi.org/10.1109/TPS.2005.856513.

[10] S.G. Davydov, A.N. Dolgov, T.I. Kozlovskaya, V.O. Revazov, V.P. Seleznev, R.K. Yakubov, Process of commutation of a vacuum electric-discharge gap by laser plasma, Plasma Phys. Rep. 42 (2016) 91–95, https://doi.org/10.1134/S1063780X16010049.

[11] A. Mazzi, F. Gorrini, A. Miotello, Single pulse excimer laser nanostructuring of thin silicon films: nanosharp cones formation and a heat transfer problem, Appl. Surf. Sci. 418 (2017) 601–606, https://doi.org/10.1016/j.apsusc.2016.09.006.

[12] Q. Suan, H. Jiang, Y. Liu, Z. Wu, H. Yang, Q. Gong, Measurement of the collision time of dense electronic plasma induced by a femtosecond laser in fused silica, Opt. Lett. 30 (2005) 320–322, https://doi.org/10.1364/OL.30.000320.

[13] Y. Mori, H. Kuwabara, K. Ishii, R. Hanayama, T. Kawashima, Y. Kitagiwa, Head-On inverse Compton scattering X-rays with energy beyond 10 keV from laser-accelerated quasi-monoenergetic electron bunches, Appl. Phys. Express 5 (2012), https://doi.org/10.1143/APEX.5.056401 056401–(1-3).

[14] Y. Hayasaki, S. Fukuda, S. Hasegawa, S. Juodkazis, Two-color pump-probe interferometry of ultra-fast light-matter interaction, Sci. Rep. 7 (2017), https://doi.org/10.1038/s41598-017-10709-z 10405–(1-8).

[15] T. Ogitsu, Y. Ping, A. Correa, B. Cho, P. Heimann, E. Schwegler, J. Cao, G. Collins, Ballistic electron transport in non-equilibrium warm dense gold, High Energy Density Phys. 8 (2012) 303–307, https://doi.org/10.1016/j.hedp.2012.01.002.

[16] B. Albertazzi, N. Ozaki, V. Zhakhovsky, A. Faenov, H. Habara, M. Harmand, N. Hartley, D. Ilnitsky, N. Inogamov, Y. Inubushi, T. Ishikawa, T. Katayama, T. Koyama, M. Koenig, A. Krygier, T. Matsuoka, S. Matsuyama, E. McBride, K.P. Migdal, G. Morard, H. Ohashi, T. Okuchi, T. Pikuz, N. Purevjav, O. Sakata, Y. Sano, T. Sato, T. Sekine, Y. Seto, K. Takahashi, K. Tanaka, Y. Tange, T. Togashi, K. Tono, Y. Umeda, T. Vinci, M. Yabashi, T. Yabuuchi, K. Yamauchi, H. Yumoto, R. Kodama, Dynamic fracture of tantalum under extreme tensile stress, Sci. Adv. 3 (2017), https://doi.org/10.1126/sciadv.1602705 e1602705–(1-6).

[17] X. Chen, T. Xue, D. Liu, Q. Yang, B. Luo, M. Li, X. Li, J. Li, Graphical method for analyzing wide-angle X-ray diffraction, Rev. Sci. Instrum. 89 (2018) 013904, https://doi.org/10.1063/1.5003452.

[18] S. Anisimov, B. Kapeliovich, T. Perel'man, Electron emission from metal surfaces exposed to ultrashort laser pulses, J. Exp. Theor. Phys. 39 (1974) 375–377.

[19] Z. Lin, L.V. Zhigilei, V. Celli, Electron-phonon coupling and electron heat capacity of metals under conditions of strong electron-phonon nonequilibrium, Phys. Rev. B: Condens. Matter Mater. Phys. 77 (2008), https://doi.org/10.1103/PhysRevB.77.075133 075133–(1-17).

[20] M. Povarnitsyn, N. Andreev, E. Apfelbaum, T. Itina, K. Khishchenko, O. Kostenko, P. Levashov, M. Veysman, A wide-range model for simulation of pump-probe experiments with metals, Appl. Surf. Sci. 258 (2012) 9480–9483, https://doi.org/10.1016/j.apsusc.2011.07.017.

[21] K.P. Migdal, Y.V. Petrov, D.K. Il'nitsky, V.V. Zhakhovsky, N.A. Inogamov, K.V. Khishchenko, D.V. Knyazev, P. Levashov, Heat conductivity of copper in two-temperature state, Appl. Phys. Mater. Sci. Process. 122 (2016) 408–412, https://doi.org/10.1007/s00339-016-9757-8.

[22] J.J. Gilvarry, Thermodynamics of the Thomas-Fermi atom at low temperature, Phys. Rev. 96 (1954) 934–943, https://doi.org/10.1103/PhysRev.96.934.

[23] J.J. Gilvarry, G.H. Peebles, Solutions of the temperature-perturbed Thomas-Fermi equation, Phys. Rev. 99 (1955) 550–556, https://doi.org/10.1103/PhysRev.99.550.

[24] P.B. Allen, Theory of thermal relaxation of electrons in metals, Phys. Rev. Lett. 59 (1987) 1460–1464, https://doi.org/10.1103/PhysRevLett.59.1460.

[25] M.I. Kaganov, I.M. Lifshitz, M. Tanatarov, Relaxation between electrons and the crystalline lattice, J. Exp. Theor. Phys. 4 (1957) 173–178.

[26] A.O. Er, J. Chen, J. Tang, P.M. Rentzepis, Coherent acoustic wave oscillations and melting on Ag(111) surface by time resolved X-ray diffraction, Appl. Phys. Lett. 100 (2012) 151910–151916, https://doi.org/10.1063/1.3703122.

[27] S.I. Anisimov, B. Rethfeld, Theory of ultrashort laser pulse interaction with a metal, Proc. SPIE 3093 (1997) 192–203, https://doi.org/10.1117/12.271674.

[28] M.P. Desjarlais, J.D. Kress, L.A. Collins, Electrical conductivity for warm, dense aluminum plasmas and liquids, Phys. Rev. E 66 (2002), https://doi.org/10.1103/PhysRevE.66.025401 025401–(1-4).

[29] V. Recoules, J.-P. Crocombette, *Ab initio* determination of electrical and thermal conductivity of liquid aluminum, Phys. Rev. B: Condens. Matter Mater. Phys. 72 (2005) 104202–104208, https://doi.org/10.1103/PhysRevB.72.104202.

[30] P.A. Zhilyaev, G.E. Norman, V.V. Stegailov, *Ab initio* calculations of thermal conductivity of metals with hot electrons, Dokl. Phys. 58 (2013) 334–338, https://doi.org/10.1002/ctpp.201200100.

[31] D. Knyazev, P. Levashov, Transport and optical properties of warm dense aluminum in the two-temperature regime: *ab initio* calculation and semiempirical approximation, Phys. Plasmas 21 (2014) 073302–073314, https://doi.org/10.1063/1.4891341.

[32] D. Alfe, M. Pozzo, M.P. Desjarlais, Lattice electrical resistivity of magnetic bcc iron from first-principles calculations, Phys. Rev. B: Condens. Matter Mater. Phys. 85 (2012) 024102–024107, https://doi.org/10.1103/PhysRevB.85.024102.

[33] Y.V. Petrov, N.A. Inogamov, K.P. Migdal, Thermal conductivity and the electron-ion heat transfer coefficient in condensed media with a strongly excited electron subsystem, JETP Lett. 97 (2013) 20–27, https://doi.org/10.1134/S0021364013010098.

[34] N. Ashcroft, N. Mermin, Solid State Physics, Vol. 1, Holt, Rinehart and Winston, 1976.

[35] A.A. Ovechkin, P.A. Loboda, A.L. Falkov, Transport and dielectric properties of dense ionized matter from the average-atom RESEOS model, High Energy Density Phys. 20 (2016) 38–54, https://doi.org/10.1016/j.hedp.2016.08.002.

[36] B. Wilthan, C. Cagran, G. Pottlacher, Combined DSC and pulse-heating measurements of electrical resistivity and enthalpy of platinum, iron, and nickel, Int. J. Thermodyn. 25 (2004) 1519–1534, https://doi.org/10.1007/s10765-004-5756-7.

[37] J. Clerouin, P. Noiret, V. Korobenko, A.D. Rakhel, Direct measurements and *ab initio* simulations for expanded fluid aluminum in the metal-nonmetal transition range, Phys. Rev. B 78 (2008), https://doi.org/10.1103/PhysRevB.78.224203 224203–(1-7).

[38] D.V. Knyazev, Calculation of Electroresistivity, Heat Conductivity and Optical Properties of Dense Plasmas on the Basis of Quantum Molecular Dynamics and

Kubo-Greenwood Formula (in Russian), Ph.D. thesis Joint Institute of High Temperatures, 2015.
[39] G. Kresse, J. Furthmuller, Efficient iterative schemes for *ab initio* total-energy calculations using a plane-wave basis set, Phys. Rev. B: Condens. Matter Mater. Phys. 54 (1996) 11169–11173, https://doi.org/10.1103/PhysRevB.54.11169.
[40] G. Kresse, D. Joubert, From ultrasoft pseudopotentials to the projector augmented-wave method, Phys. Rev. B: Condens. Matter Mater. Phys. 59 (1999) 1758–1764, https://doi.org/10.1103/PhysRevB.59.1758.
[41] P. Bloechl, Projector augmented-waves method, Phys. Rev. B: Condens. Matter Mater. Phys. 50 (1994) 17953–17962, https://doi.org/10.1103/PhysRevB.50.17953.
[42] J.P. Perdew, K. Burke, M. Ernzerhof, Generalized gradient approximation made simple, Phys. Rev. Lett. 77 (18) (1996) 3865–3869, https://doi.org/10.1103/PhysRevLett.3865.
[43] M. Gajdos, K. Hummer, G. Kresse, Linear optical properties in the projector-augmented wave methodology, Phys. Rev. B: Condens. Matter Mater. Phys. 73 (2006), https://doi.org/10.1103/PhysRevB.73.045112 045112–(1-9).
[44] D.V. Knyazev, P.R. Levashov, *Ab initio* calculation of transport and optical properties of aluminum: influence of simulation parameters, Comput. Mater. Sci. 79 (2013) 817–829, https://doi.org/10.1016/j.commatsci.2013.04.066.
[45] D.V. Knyazev, P.R. Levashov, Thermodynamic, transport, and optical properties of dense silver plasma calculated using the GreeKuP code, Contrib. Plasma Phys. (2018) 1–9, https://doi.org/10.1002/ctpp.201800084.
[46] M.J. Kramer, M.I. Mendelev, M. Asta, Structure of liquid Al and $Al_{67}Mg_{33}$ alloy: comparison between experiment and simulation, Philos. Mag. 94 (2014) 1876–1892, https://doi.org/10.1080/14786435.2014.886786.
[47] H. Fujii, S. Tahara, Y. Kato, S. Kohara, M. Itou, Y. Kawakita, S. Takeda, Structural properties of liquid Au-Si and Au-Ge alloys with deep eutectic region, J. Non-Cryst. Solids 353 (2007) 2094–2098, https://doi.org/10.1016/j.jnoncrysol.2007.02.031.
[48] D. Holland-Moritz, O. Heinen, R. Bellisent, T. Schenk, Short-range order of stable and undercooled liquid titanium, Mater. Sci. Eng. A 449-451 (2007) 42–45, https://doi.org/10.1016/j.msea.2005.12.093.
[49] T.H. Kim, G.W. Lee, B. Sieve, A.K. Gangopadhyay, R.W. Hyers, T.J. Rathz, J.R. Rogers, D.S. Robinson, K.F. Kelton, A.I. Goldman, In situ high-energy X-ray diffraction study of the local structure of supercooled liquid Si, Phys. Rev. Lett. 95 (2005), https://doi.org/10.1103/PhysRevLett.95.085501 085501–(1-4).
[50] H. Kimura, M. Watanabe, K. Izumi, T. Hibiya, D. Holland-Moritz, T. Schenk, S.S.K.R. Bauchspiess, I. Egry, K. Funakoshi, M. Hanfland, X-ray diffraction study of undercooled molten silicon, Appl. Phys. Lett. 78 (2001) 604–606, https://doi.org/10.1063/1.1341220.
[51] R.C. Remsing, M.L. Klein, J. Sun, Refined description of liquid and supercooled silicon from *ab initio* simulations, Phys. Rev. B 97 (2018), https://doi.org/10.1103/PhysRevB.97.140103 140103–(1-5).
[52] L. Harbour, G.D. Forster, M.W.C. Dharma-wardana, L.J. Lewis, Ion-ion dynamic structure factor, acoustic modes, and equation of state of two-temperature warm dense aluminum, Phys. Rev. E 97 (2018), https://doi.org/10.1103/PhysRevE.97.043210 043210–(1-10).
[53] R. Darkins, P.-W. Ma, S.-T. Murphy, D.M. Duffy, Simulating electronically driven structural changes in silicon with two-temperature molecular dynamics, Phys. Rev. B: Condens. Matter Mater. Phys. 98 (2018), https://doi.org/10.1103/PhysRevB.98.024304 024304–(1-11).
[54] V. Zhakhovskii, N. Inogamov, Y. Petrov, S. Ashitkov, K. Nishihara, Molecular dynamics simulation of femtosecond ablation and spallation with different interatomic potentials, Appl. Surf. Sci. 255 (2009) 9592–9596, https://doi.org/10.1016/j.apsusc.2009.04.082.
[55] S. Plimpton, Fast parallel algorithms for short-range molecular dynamics, J. Comput. Phys. 117 (1995) 1–19, https://doi.org/10.1006/jcph.1995.1039.
[56] Y.V. Petrov, K.P. Migdal, D.V. Knyazev, N.A. Inogamov, P.R. Levashov, Transport properties of copper with excited electron subsystem, J. Phys. Conf. Ser. 774 (2016), https://doi.org/10.1088/1742-6596/774/1/012103 012103–(1-18).
[57] Elk is an all-electron full-potential linearised augmented-planewave (FP-LAPW) code released under either the GNU General Public License (GPL) or the GNU Lesser General Public License (LGPL). Elk code is available on http://elk.sourceforge.net.
[58] T. Hüpf, C. Cagran, G. Pottlacher, Thermophysical properties of 22 pure metals in the solid and liquid state — the pulse-heating data collection, EPJ Web of Conferences 15 (2011), https://doi.org/10.1051/epjconf/20111501018 01018–(1-5).
[59] A.D. Cicco, A. Trapananti, Study of local icosahedral ordering in liquid and undercooled liquid copper, J. Non-Cryst. Solids 353 (2007) 3671–3678, https://doi.org/10.1016/j.jnoncrysol.2007.05.150.
[60] J.M. Ziman, The electron transport properties of pure liquid metals, Adv. Phys. 16 (1967) 551–580, https://doi.org/10.1080/00018736700101665.
[61] Treatise on Process Metallurgy, in: S. Seetharaman (Ed.), Vol. 1 Elsevier, 2014.
[62] J. Sun, A. Ruzsinszky, J.P. Perdew, Strongly constrained and appropriately normed semilocal density functional, Phys. Rev. Lett. 115 (2015), https://doi.org/10.1103/PhysRevLett.115.036402 036402–(1-5).
[63] J. Sun, R.C. Remsing, Y. Zhang, Z. Sun, A. Ruzsinszky, H. Peng, Z. Yang, A. Paul, U. Waghmare, X. Wu, M.L. Klein, J.P. Perdew, Accurate first-principles structures and energies of diversely bonded systems from an efficient density functional, Nat. Chem. 8 (2016) 831–836, https://doi.org/10.1038/nchem.2535.
[64] T. Okada, S. Ohno, Electrical properties of liquid Si and liquid Au-Si alloys, J. Phys. Soc. Jpn. 72 (2003) 352–356, https://doi.org/10.1143/JPSJ.72.352.
[65] C. Lee, W. Yang, R.G. Parr, Development of the Colle-Salvetti correlation-energy formula into a functional of the electron density, Phys. Rev. B: Condens. Matter Mater. Phys. 37 (1988) 785–789, https://doi.org/10.1103/PhysRevB.37.785.
[66] A.D. Becke, Density-functional exchange-energy approximation with correct asymptotic behavior, Phys. Rev. A 38 (1988) 3098–3100, https://doi.org/10.1103/PhysRevA.38.3098.
[67] J. Heyd, G. Scuseria, M. Ernzerhof, Hybrid functionals based on a screened Couloumb potential, J. Chem. Phys. 118 (2003) 8207–8216, https://doi.org/10.1063/1.1564060.
[68] J. Heyd, G. Scuseria, M. Ernzerhof, Erratum: Hybrid functionals based on a screened Couloumb potential (J. Chem. Phys. 118, 8207 (2003)), J. Chem. Phys. 124 (2006), https://doi.org/10.1063/1.22044597 219906–219906.
[69] G.S. Khara, S.T. Murphy, S.L. Daraszewicz, D.M. Duffy, The influence of the electronic specific heat on swift heavy ion irradiation simulations of silicon, J. Phys. Condens. Matter 28 (2016), https://doi.org/10.1088/0953-8984/28/39/395201 395201–(1-7).
[70] B.B.L. Witte, P. Sperling, M. French, V. Recoules, S.H. Glenzer, R. Redmer, Observations of non-linear plasmon damping in dense plasmas, Phys. Plasmas 25 (2018), https://doi.org/10.1064/1.5017889 056901–(1-10).
[71] Y.B. Magomedov, G.G. Gadjiev, High-temperature thermal conductivity of silicon in the solid and liquid states, High Temp. 46 (2008) 422–424, https://doi.org/10.1134/S0018151X08030206.
[72] T. Nishi, H. Shibata, H. Ohta, Thermal diffusivities and conductivities of molten germanium and silicon, Mater. Trans. 44 (2003) 2369–2374, https://doi.org/10.2320/matertrans.44.2369.
[73] J.P. Perdew, Y. Wang, Accurate and simple analytic representation of the electron-gas correlation energy, Phys. Rev. B: Condens. Matter Mater. Phys. 45 (1991) 13244–13249, https://doi.org/10.1103/PhysRevB.45.13244.
[74] Z.h. Yang, J.R. Trail, A. Pribram-Jones, K. Burke, R.J. Needs, C.A. Ullrich, Exact and approximate Kohn-Sham potentials in ensemble density-functional theory, Phys. Rev. A: At. Mol. Opt. Phys. 90 (2014), https://doi.org/10.1103/PhysRevA.90.042501 042501–(1-8).
[75] V.V. Karasiev, L. Calderin, S.B. Trickey, Importance of finite-temperature exchange correlation for warm dense matter calculations, Phys. Rev. B: Condens. Matter Mater. Phys. 93 (2016), https://doi.org/10.1103/PhysRevE.93.063207 063207–(1-12).
[76] K. Migdal, Y. Petrov, N. Inogamov, Kinetic coefficients for d-band metals in two-temperature states created by femtosecond laser irradiation, Proc. SPIE 9065 (2013) 906503–906517, https://doi.org/10.1117/12.2053172.
[77] F. Knider, J. Hugel, A.V. Postnikov, *Ab initio* calculation of dc resistivity in liquid Al, Na and Pb, J. Phys. Condens. Matter 19 (2007), https://doi.org/10.1088/0953-8984/19/19/196105 196105–(1-12).
[78] S. Mazevet, M. Torrent, V. Recoules, F. Jollet, Calculations of the transport properties within the PAW formalism, High Energy Density Phys. 6 (2010) 84–88, https://doi.org/10.1016/j.hedp.2009.06.004.
[79] H. Reinholz, G. Ropke, S. Fosmej, R. Redmer, Conductivity of warm dense matter including electron-electron collisions, Phys. Rev. E 91 (2015), https://doi.org/10.1103/PhysRevE.91.043105 043105–(1-17).
[80] C. Ambrosch-Draxl, J.O. Sofo, Linear optical properties of solids within the full-potential linearized augmented planewave method, Comput. Phys. Commun. 175 (2006) 1–14, https://doi.org/10.1016/j.cpc.2006.03.005.
[81] M. Cazzaniga, L. Caramella, N. Manini, G. Onida, *Ab initio* intraband contributions to the optical properties of metals, Phys. Rev. B: Condens. Matter Mater. Phys. 82 (2010), https://doi.org/10.1103/PhysRevB.82.035104 035104–(1-7).
[82] E.P. Silaeva, E. Bevillon, R. Stoian, J.P. Colombier, Ultrafast electron dynamics and orbital-dependent thermalization in photoexcited metals, Phys. Rev. B: Condens. Matter Mater. Phys. 98 (2018), https://doi.org/10.1103/PhysRevB.98.094306 094306–(1-8).
[83] M. Berrada, R.A. Secco, W. Yong, Decreasing electrical resistivity of gold along the melting boundary up to 5 GPa, High Pressure Res. 38 (2018) 367–376, https://doi.org/10.1080/09857959.2018.1493476.
[84] R. Brandt, G. Neuer, Electrical resistivity and thermal conductivity of pure aluminum alloys up to and above the melting temperature, Int. J. Thermophys. 28 (2007) 1429–1446, https://doi.org/10.1007/s10765-006-0144-0.
[85] M. Leitner, T. Leitner, A. Schmon, K. Aziz, G. Pottlacher, Thermophysical properties of liquid aluminum, Metall. Mater. Trans. A 48 (2017) 3036–3045, https://doi.org/10.1007/s11661-017-4053-6.
[86] M.E. Povarnitsyn, K.V. Khishchenko, P.R. Levashov, Phase transitions in femtosecond laser ablation, Appl. Surf. Sci. 255 (2009) 5120–5124, https://doi.org/10.1016/j.apsusc.2008.09.199.
[87] K. Boboridis, Application of Single-wavelength Radiation Thermometry and High-speed Laser Polarimetry to Thermophysical Property Measurements on Pulse-heated Metals, Ph.D. thesis National Institute of Standards and Technology, Technische Universitat Graz, 2001.